Topics in Catalysis
https://doi.org/10.1007/s11244-024-01935-7

ORIGINAL PAPER

CO_2 Conversion via Low-Temperature RWGS Enabled by Multicomponent Catalysts: Could Transition Metals Outperform Pt?

G. Torres-Sempere[1] · J. González-Arias[1] · A. Penkova[1] · J. L. Santos-Muñoz[1] · L. F. Bobadilla[1] · J. A. Odriozola[1] · L. Pastor-Pérez[1] · T. R. Reina[1]

Accepted: 26 February 2024

Abstract
In the context of CO_2 valorisation, the reverse water–gas shift reaction (RWGS) is gathering momentum since it represents a direct route for CO_2 reduction to CO. The endothermic nature of the reaction posses a challenge when it comes to process energy demand making necessary the design of effective low-temperature RWGS catalysts. Herein, multicomponent Cs-promoted Cu, Ni and Pt catalysts supported on TiO_2 have been studied in the low-temperature RWGS. Cs resulted an efficient promoter affecting the redox properties of the different catalysts and favouring a strong metal-support interaction effect thus modulating the catalytic behaviour of the different systems. Positive impact of Cs is shown over the different catalysts and overall, it greatly benefits CO selectivity. For instance, Cs incorporation over Ni/TiO_2 catalysts increased CO selectivity from 0 to almost 50%. Pt-based catalysts present the best activity/selectivity balance although $CuCs/TiO_2$ catalyst present comparable catalytic activity to Pt-studied systems reaching commendable activity and CO selectivity levels, being an economically appealing alternative for this process.

Keywords Low-temperature RWGS · CO_2 valorization · Noble metal · Cs promoter · Cu-based catalyst · Circular economy · CCU

1 Introduction

Over the past decades, the continuous rise in CO_2 levels has made it one of the most problematic greenhouse gases (GHGs) [1]. Carbon Capture and Utilization (CCU) technologies have emerged as highly effective solutions for reducing CO_2 concentrations and harnessing its potential [2]. These technologies enable the transformation of CO_2 into valuable chemicals like CO or CH_4, facilitating a circular economy that promotes a smarter utilization of natural resources [3]. Among CCU paths, syngas production from CO_2 is a very promising route since syngas is a precursor for many fuels (i.e., methanol, formic acid or light olefins) [4]. Syngas can be produced from CO_2 and H_2 via the reverse water–gas shift (RWGS) reaction [5]. This path allows to valorise large quantities of CO_2 due to the high CO_2 conversion and low H_2 consumption of the RWGS compared with other CO_2 hydrogenation reactions [6].

The RWGS consists of the hydrogenation of CO_2 to form CO and H_2O (Eq. 1) [7]. The RWGS is an endothermic reaction. In other words, CO production via RWGS is favoured at high temperatures. Nonetheless, there are also other side reactions competing with the RWGS[8]. These are the Sabatier reaction (Eq. 2) and the CO methanation reaction (Eq. 3). Both are exothermic, being therefore favoured at low temperatures [9]. Besides these unavoidable side reactions, the high stability of CO_2 makes necessary the synthesis of a high selective and active catalyst.

$$CO_2(g) + H_2(g) \rightarrow CO(g) + H_2O(g) \quad \Delta H_2^\circ \ 42.1 \text{ kJ/mol} \tag{1}$$

$$CO_2(g) + 4H_2(g) \rightarrow CH_4(g) + 2H_2O(g) \quad \Delta H_2^\circ \ -65 \text{kJ/mol} \tag{2}$$

$$CO(g) + 3H_2(g) \rightarrow CH_4(g) + H_2O(g) \quad \Delta H_2^\circ \ -206 \text{ kJ/mol} \tag{3}$$

✉ G. Torres-Sempere
gtorres1@us.es

✉ T. R. Reina
tramirez@us.es

[1] Inorganic Chemistry Department and Materials Sciences Institute, University of Seville-CSIC, Seville, Spain

Published online: 02 April 2024

Using the RWGS reaction at low temperatures is especially appealing due to its clear energy-saving benefits and its compatibility with downstream processes, such as methanol production, which typically occurs at temperatures around 300 °C [10]. Several attempts to explore the RWGS at low temperature have been described in literature [11–14]. Among the different supports that have been studied for this process (i.e., Al_2O_3 [15], CeO_2 [16], SiO_2 [17]), TiO_2 stands out for its redox properties, providing oxygen vacancies that facilitate the activation and reduction of CO_2. Another advantage of TiO_2 is the strong metal–support interaction (SMSI), which enhances the number of reduction sites on the TiO_2 surface [18]. Many noble metals have been studied as the active phase for RWGS catalysts due to their high catalytic activity and selectivity (i.e., Rh [19], Pd [20], Au [21]). However, the high cost associated with these metals has limited their industrial-scale application. Cu has also been studied as an active phase in this reaction, offering a more economically viable alternative to noble metals. Even though Cu stands as a very promising alternative, Cu-based catalysts exhibit lower catalytic activity, particularly for low-temperature reactions. Additionally, long-term experiments have revealed surface sintering of the catalyst, diminishing its lifespan [22]. To overcome these issues, research on new Cu catalytic systems is needed.

Despite the recent efforts of the catalysis community working on the RWGS reaction, there are still many challenges when facing low temperature reaction performance. To shade a bit of light to this intriguing reaction, in this work we explore the use of effective multicomponent catalysts using Cs as promoter that our team identified as a very promising dopant [23]. Indeed, Cs possesses a large ionic radius, low ionization potential, and excellent basic properties. Its electropositive character facilitates CO_2 activation [23]. To examine the influence of Cs, we adopt the following approach. Firstly, we synthesize Cu/TiO_2 and $Cu–Cs/TiO_2$ catalysts and evaluate their catalytic performance. Subsequently, Pt/TiO_2 and $Pt–Cs/TiO_2$ catalysts are also synthesized and studied in order to compare the catalytic performance of Cu with a well-known noble metal for this process [24, 25]. Furthermore, we explore the impact of Cs on Ni-based catalysts. As Ni exhibits high activity in methanation reaction [26], we aim to ascertain the ability of Cs to inhibit methanation and promote CO production. To achieve this, we prepare Ni/TiO_2 and $Ni–Cs/TiO_2$ catalysts for comparison.

Under these premises, this work presents a comparative study of transition metals (Cu, Ni) vs noble metal (Pt) based catalysts for the low-temperature RWGS analysing the impact of Cs as a dopant. Activity–structure/chemical properties correlations are discussed along with lessons learned in the design of low-temperature RWGS catalysts that could play a role in the urgent challenge of industrial decarbonisation.

2 Experimental

2.1 Catalyst Preparation

The TiO_2 supported catalysts were prepared by the sequential wet impregnation method using a commercial TiO_2-P25 (Degussa) support. First, the TiO_2 was washed with deionized water, filtered and dried for 48 h at 115 ºC. Then, the washed TiO_2 was calcinated at 550 ºC during 3 h. Once the support was calcinated, the active phases were impregnated. The right amount of H_2PtCl_6, $Ni(NO_3)_2{\cdot}6H_2O$ and $Cu(NO_3)_2{\cdot}5H_2O$ was dissolved in excess of water to obtain 1 wt% Pt, 10 wt% Ni and 10 wt% Cu respectively. Different loads of the active metals in the catalyst were selected due to the different properties of those. For instance, only 1 wt.% of Pt was used due to its high reactivity and high cost compared to Cu and Ni. Afterwards, the samples were dried for 48 h at 115 ºC and calcinated for 3 h at 550 ºC. Finally, for the Cs-doped samples, the right amount of Cs_2CO_3 was impregnated on the $Pt–TiO_2$, $Ni–TiO_2$ and $Cu–TiO_2$ samples to get a 2.5 wt% of Cs. Then, the samples were dried and calcinated under the same conditions (i.e., 3 h and 550 °C).

2.2 Catalyst Characterization

The as-prepared catalysts were characterized by X-ray diffraction (XRD) with an X'Pert Pro PANalytical at room temperature using Cu-K (40 mA, 45 kV) over a 2-theta range of 10°–90°. The textural characterization of the catalysts was carried out by N_2 adsorption at − 196 °C with an AUTOSORB-6 equipment (QUANTACHROME INSTRUMENTS). Catalysts were first outgassed at 250 ºC for 2 h.

The H_2 temperature-programmed reduction (TPR) was performed using a conventional U-shaped quartz reactor connected to a thermal conductivity detector (TCD). A gas flow of 50 mL/min consisting of 5% H_2 diluted in Ar was passed through the reactor. TPR experiments were conducted using approximately 100 mg of catalysts for Cu and Ni, while 150 mg was used for Pt due to its lower weight percentage. The heating rate was set at 10 ºC/min, gradually increasing the temperature from room temperature to 900 ºC.

The investigation of particle size and morphology of the active phases was conducted using transmission electron microscopy (TEM) on a JEOL 2100Plus microscope operating at 200 kV. The microscope was equipped with an Energy Dispersive X-Ray analysis system (EDX X-Max 80 T, Oxford Instruments) and a CCD camera for image recording.

High-resolution TEM (HR-TEM) analysis was performed on a FEI Talos F200S electron microscope, utilizing an acceleration voltage of 200 kV, a field emission filament, and a side-mounted Ceta 16 M camera.

The XPS experiments were conducted on a SPECS photoelectron spectrometer equipped with a PHOIBOS 150 MCD analyzer operating at a constant pass energy of 35 eV and a resolution of 0.1 eV. The X-ray radiation source used was Kα emission generated by bombarding an aluminum target with electrons at an energy of hν = 1486.6 eV and a bandwidth of 0.85 eV, operating at 250 W and maintaining a potential of 12.5 kV. Due to significant overlap with CsMNN, Cu catalysts utilized a Mg source with an energy of hν = 1253.6 eV and a bandwidth of 0.7 eV, operating at 150 W and maintaining a potential of 10 kV. The analysis chamber operated under ultra-high vacuum conditions, with a pressure of 10^{-10} mbar.

2.3 Catalytic Activity

The RWGS reaction was carried out in a vertical continuous fixed-bed reactor where 0.2 g of each catalyst was placed in the middle of a quartz reactor. Initially, the catalyst was first activated by heating the reactor up to 500 ºC under a H_2/N_2 gas mixture (5/45). Subsequently, the temperature was reduced to 300 ºC using a N_2 gas flow. Following this, the catalyst was exposed to a feed gas mixture of H_2:CO_2 in a ratio of 4:1, while maintaining a weight hourly space velocity (WHSV) of 30,000 mL/g h The catalytic tests were performed at temperatures of 300, 400 and 500 ºC for 1 h at each temperature. The products of the reaction were analysed using gas chromatography integrated with flame ionization (FID) and thermal conductivity (TCD) detectors. CO_2 conversion (Eq. 4), CO selectivity (Eq. 5) CH_4 selectivity (Eq. 6) and specific activity towards CO (Eq. 7) and CH_4 (Eq. 8) were utilized as parameters to compare the catalytic activity of the different samples.

$$\mathrm{CO_2\ Conversion\ (\%)} = \left(\frac{\left[\mathrm{CO_2}\right]_{in} - \left[\mathrm{CO_2}\right]_{out}}{\left[\mathrm{CO_2}\right]_{in}} \right) \times 100 \quad (4)$$

$$\mathrm{CO\ Selectivity\ (\%)} = \left(\frac{[\mathrm{CO}]_{out}}{\left[CH_4\right]_{out} + [\mathrm{CO}]_{out}} \right) \times 100 \quad (5)$$

$$\mathrm{CH_4\ Selevticity\ (\%)} = \left(\frac{\left[\mathrm{CH_4}\right]_{out}}{\left[\mathrm{CH_4}\right]_{out} + [\mathrm{CO}]_{out}} \right) \times 100 \quad (6)$$

$$\textit{Specific activity to CO} = \left(\frac{molCO/h}{\mathrm{gcat}} \right) \quad (7)$$

$$\textit{Specific activity to CH4} = \left(\frac{\mathrm{mol}CH_4/\mathrm{h}}{\mathrm{gcat}} \right) \quad (8)$$

2.3.1 Equilibrium Limits Calculation

ChemStations' ChemCad software package was used to observe the thermodynamic limits of the RWGS reactions over a range of temperatures. The Soave–Redlich–Kwong equation of state was used in a Gibbs reactor. Material flows into the reactor are identical to those intended to be used for experimentation.

3 Results and Discussion

3.1 XRD

XRD analysis was conducted to determine the crystalline phases present in our catalytic systems. Figure 1 displays the XRD results for the six catalysts as well as the calcined support. For sake of clarity, the crystalline phases that are common to all XRD profiles are marked in the support profile, while the newly observed phases are indicated in the pattern above, in Fig. 1.

Upon calcination of TiO_2 at 550 ºC, both anatase and rutile crystalline phases are observed, being anatase more predominant. The presence of these two phases in Pt/TiO_2 catalysts has also been previously identified by other researchers [27]. Previous works point out that the lack of diffraction lines corresponding to the Pt phase in the 1% Pt/TiO_2 catalyst indicates that Pt is indeed well dispersed throughout the catalyst. This fact can also be confirmed by the HR-TEM results (see Sect. 3.3), where the crystalline Pt particles on TiO_2 cannot be clearly distinguished. This can also be ascribed to the low Pt loading which is below the detection limit of the equipment. It is noteworthy that the addition of the active phase and the promoter leads to an increase of the rutile phase in all catalysts. This could be explained by the repeated calcination of the samples due to the nature of the synthesis, as the conversion from anatase to rutile initiates at temperatures exceeding 500 ºC [28]. The absence of Cs peaks in the XRD patterns of the different Cs-doped catalysts suggests that the Cs species are either in an amorphous state or very well dispersed on the prepared catalysts. This could also be due to the low concentration of Cs.

Apart from the anatase and rutile phases from the TiO_2 support, the XRD patterns for the Ni and Ni-Cs catalysts reveal the presence of NiO_2 and $NiTiO_3$ peaks. The $NiTiO_3$ phase is more predominant in the Cs-doped catalyst, as clearly observed in Fig. 1B indicating the impact of Cs

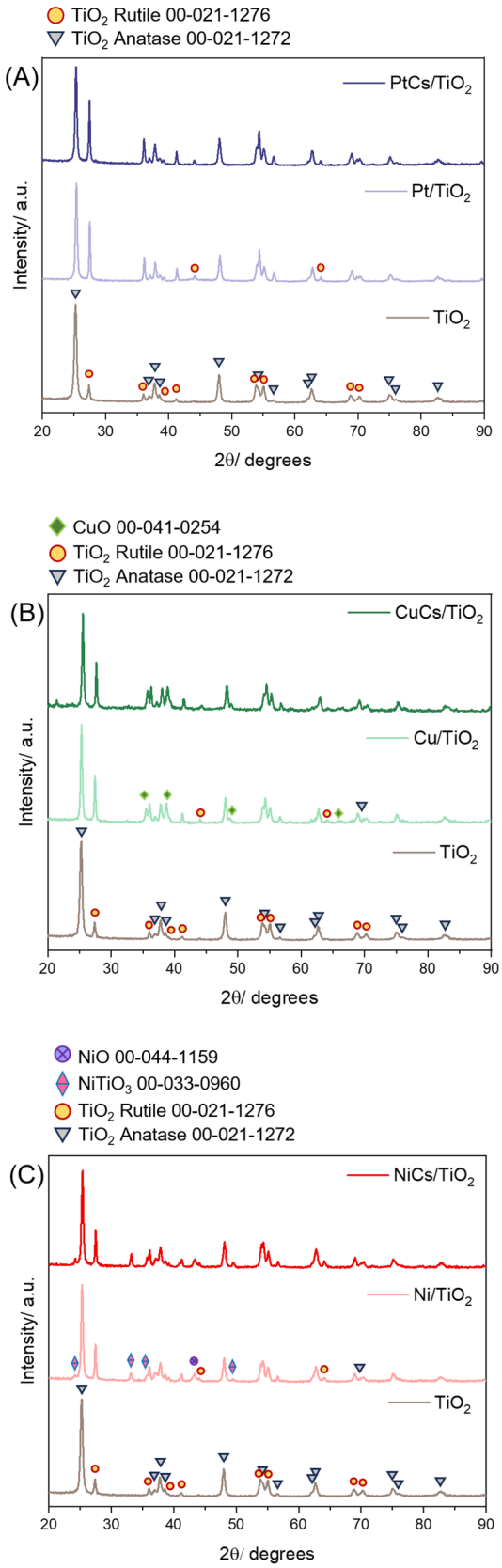

Fig. 1 Powder XRD patterns of calcinated samples: **A** TiO_2, Cu/TiO_2 and $CuCs/TiO_2$; **B** TiO_2, Ni/TiO_2 and $NiCs/TiO_2$; and **C** TiO_2, Pt/TiO_2 and $PtCs/TiO_2$

Table 1 BET, pore volume and pore diameter of the calcinated samples

Catalyst	BET (m^2/g)	Pore volume (cm^2/g)	Pore diameter (A)
TiO_2–P25	50	0.39	290
Cu/TiO_2	32	0.24	308
$CuCs/TiO_2$	29	0.22	306
Ni/TiO_2	37	0.26	276
$NiCs/TiO_2$	36	0.25	287
Pt/TiO_2	49	0.31	255
$PtCs/TiO_2$	49	0.29	240

addition to the final catalysts structure. As for the Cu family, both Cu and Cs-doped Cu catalysts present a similar XRD pattern with evidences of CuO formation.

3.2 Textural Properties

Table 1 presents the specific surface area, pore volume and pore diameter of the commercial calcined TiO_2–P25 and the six synthetised catalytic systems [29]. TiO_2 is known for its relatively high surface area, which can be advantageous for catalytic reactions, providing more active sites for reactant adsorption, enhancing the catalytic activity. The addition of the active phase results in a decrease in the specific surface area of TiO_2 for Ni and Cu based catalysts. For Pt based catalysts surface area is maintained. This can be correlated to the lower Pt loading compared to that of Cu and Ni. The increased in pore diameter for all the samples could be attributed to the incorporation of the metals within the pores of the support. Cs does not seem to affect the surface area. This could suggest a high dispersion and low particle size of the promoter which is in good agreement with previous reports [18]. It can be observed that the pore diameter decreases significantly for the Pt-based catalysts while maintaining the highest pore volume. This could be explained by the fact that Pt presents the highest atomic diameter and is deposited at the pores mouth, reducing the pore diameter while preserving the pore volume. The pore diameter of the Cu-based catalysts is the largest, while the pore volume is the lowest, indicating that copper particles are likely deposited inside the pores. The situation for Ni catalysts is similar to that of copper. The six samples display similar type-IV isotherms (Fig. S1), which are characteristic of mesoporous solids [30]. These mesopores can offer improved mass transport and diffusion properties, enabling better reactant access and product desorption. To gain further insights into the textural properties, the crystallite sizes of anatase and rutile of the various catalysts have been depicted in Fig. 2. It can be observed that there is no clear trend among the samples. In the case of the Pt-based catalyst, the Cs-doped system

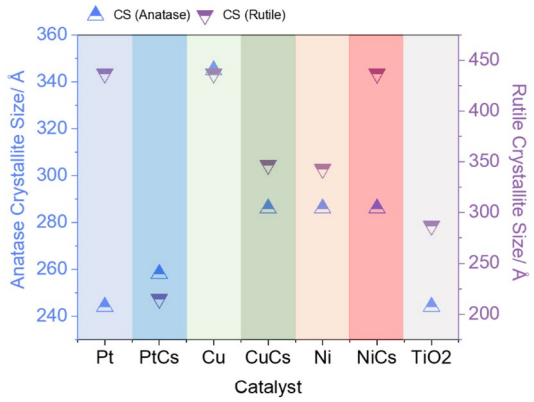

Fig. 2 Crystallite size of anatase and rutile phases for the six catalysts and the support

exhibits a significant decrease in anatase crystallite size. Additionally, this catalyst is the only sample that presents a smaller crystallite size than the bare support. For the Ni catalysts, the doped one shows an increase in rutile crystallite size. As will be discussed in the catalytic activity section, the Cu/TiO_2 catalyst is the least active sample. This may be correlated with the fact that these catalysts exhibit the highest crystallite size for the two phases indicating some sort of correlation between activity and crystal size and perhaps suggesting such large crystallite size marks a threshold for activity depletion.

3.3 HR-TEM

Figure 3 provides HR-TEM images that confirm the presence of CuO, NiO and $NiTiO_3$ as discussed in the XRD results. In addition, it appears that interplanar distances characteristic of mix copper oxide (I, II) named paramelaconite (Cu_4O_3) is present in the Cs-doped catalyst. This occurrence can be explained by the electron-donor factor of Cs, that reduces Cu species in the surfaces of the catalyst. In both the Pt/TiO_2 and $Pt–Cs/TiO_2$ samples, a remarkable dispersion of Pt particles is achieved. The particle size distribution (Fig. S2) reveals that the Pt particles in the Cs doped catalyst are about 0.1 nm, while in the non-doped catalyst, they range between 0.1 and 0.2 nm. However, in the case of the Cu and Ni catalysts, the opposite effect is observed. The Cu/TiO_2 catalyst exhibits a significant number of metallic Cu particles with a medium size smaller than 5 nm, which are absent in the Cs-doped catalyst where the medium particle size is around 22 nm (Fig. S2). A similar effect is observed in the Ni catalysts. While Ni/TiO_2 shows a medium particle size distribution between 5 and 10 nm, in the Cs-doped catalysts, it is about 21 nm. This adverse effect can be attributed to the larger loading of Cu and Ni compared to Pt catalysts. 10% of Cu and Ni is enough for Cs to make it difficult for the particles to distribute homogenously in the support surface. This effect is not observed in the $PtCs/TiO_2$ catalyst due to the lower Pt loading (1 wt%). The larger size of Cs particles helps Pt particles to be separated over the TiO_2 surface.

3.4 H_2-TPR

Redox behaviour is relevant for a redox process like the RWGS. Figure 4 shows the H_2-TPR of the six catalysts providing insights in the redox properties of the multicomponent systems. In the Ni/TiO_2 catalyst, three distinct reduction zones (low, medium, and high temperature zones) are observed, being the maximum temperatures located at 404, 508 and 602 ºC respectively. The low temperature reduction process is attributed to bulk NiO located on the surface of the support. The medium temperature reduction zone corresponds to the reduction of NiO significantly interacting with TiO_2 while the high temperature zone is associated to the reduction of $NiTiO_3$ species to Ni^0 [31]. In the case of the Cs-doped nickel catalyst, these three zones appear at higher temperatures, being the maximum temperatures at 433, 542 and 636 ºC respectively. This may indicate a stronger interaction between the NiO and $NiTiO_3$ species with the TiO_2 in the presence of Cs doping which is consistent with previous studies [32]. In addition, the presence of Cs could favour the formation of nickel hydroxide during the synthesis. This nickel hydroxide would be the precursor for the formation of $NiTiO_3$ which could explain the higher intensity of this specie in XRD. In other words, the addition of Cs impacts on the final structure and active phase of the Ni-based system [32].

Similarly, in the Cu catalyst, two reduction zones are observed with the maximum temperatures located at 140 and 208 ºC. The first reduction zone corresponds to highly dispersed copper oxide nanoparticles, while the second zone is attributed to larger copper clusters. This would be in good agreement with particle size distribution from HR-TEM, where half of the copper particles size were 1 nm for the Cu/TiO_2 sample. Normally, CuO reduction peaks appear above 300 ºC. However, the interaction between CuO and TiO_2 shifts these peaks to lower temperatures. This shift is caused by the formation of oxygen vacancies in the TiO_2 surface, leading to the generation of TiO_x species. These species attract oxygen, facilitating the reformation of TiO_2 due to its inherent instability [33]. In the Cs-doped catalysts, these two reduction zones appear at higher temperatures (220 and 293 ºC). The first zone is ascribed to the reduction of CuO species interacting with TiO_2, while the second one is likely due to bulk CuO with weaker interaction with the support. This would be also in good agreement with the particle size distribution as for the $CuCs/TiO_2$ catalysts, copper particle size is bigger in comparison with the non-doped sample.

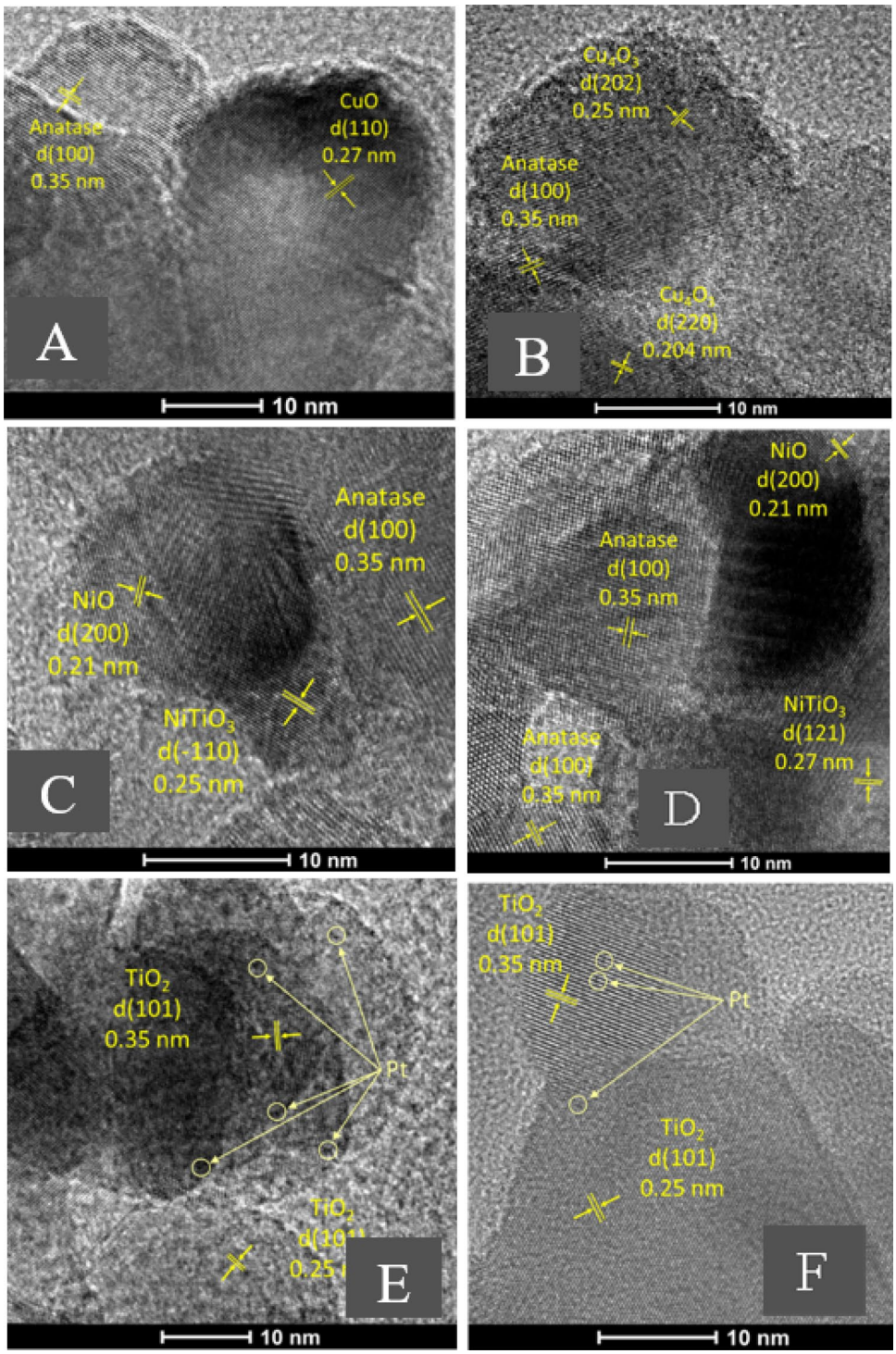

Fig. 3 HR-TEM images: **A** Cu/TiO_2; **B** CuCs/TiO_2; **C** Ni/TiO_2; **D** NiCs/TiO_2; **E** Pt/TiO_2 and **F** PtCs/TiO_2

As for the Pt/TiO_2 catalyst, two reduction zones are observed centred at 335 and 562 ºC respectively. The zone at the lower temperature corresponds to the reduction of surface oxygen of TiO_2, while the zone at the higher temperature is associated with the reduction of bulk TiO_2 [34]. The presence of Pt in the catalyst seems to facilitate the reduction of oxygen species in TiO_2, which is consistent with previous works [34]. It is reported that the addition of noble metals to oxide supports can enhance the reduction of the support because of H spill-over effect. This is explained because of the ability of H_2 dissociation of noble metals. This reduction associated with H spill-over effect could reduce TiO_2 to TiO_x promoting the SMSI effect [35]. In the Cs-doped catalyst the reduction zones

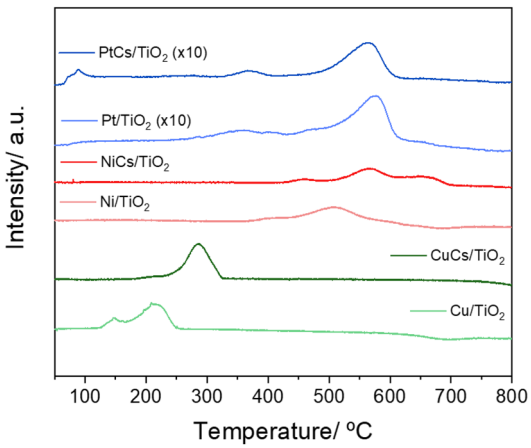

Fig. 4 TPR profile of calcinated samples

associated with the reduction of surface and bulk TiO_2 are also slightly shifted to higher temperatures (385 and 579 ºC). An additional reduction zone appears at lower temperatures. This zone is related to the reduction of PtO_x species to Pt^0 and TiO_2 species interacting strongly with Pt [18, 36]. The addition of Cs seems to promote the reduction of PtO_x to metallic Pt, as this peak is not present in the non-doped catalyst.

3.5 XPS

Figure 5 shows the XPS measurements of the six studied catalysts. Figure 5c presents the Ni2p spectra of Ni/TiO_2 and $NiCs/TiO_2$ samples. It can be observed that there is no electronic change in the presence of Cs. Ruling out the electronic effect opens the question of how Cs significantly affects the selectivity trends on Ni (and also Pt and Cu). In this sense building upon our recent operando study, we see that Cs changes the reaction pathway by neutralizing the hydroxyl groups of the TiO_2 surface, partially inhibiting methane formation [37]. When it comes to Cu and Pt, Cs does affect their surface electronic features as observed in our XPS results. Figure 5a shows Pt4d spectra for the two Pt based catalysts. The Pt/TiO_2 sample presents a maximum in binding energy at 318.3 eV that can be attributed to PtO_2 [38]. It can be observed a decrease in the binding energy of the $PtCs/TiO_2$ sample to 317.8 eV, indicating an increase in electronic density. It can be deduced that this electron density increase is due to Cs electropositive behaviour. Also as mentioned before, our recent study demonstrates how the presence of Cs neutralizes hydroxyl surface group and provides new active sites that favours CO production rather than CH_4 [37]. In addition, another potential consequence of this increase in electronic density could be to facilitate electron

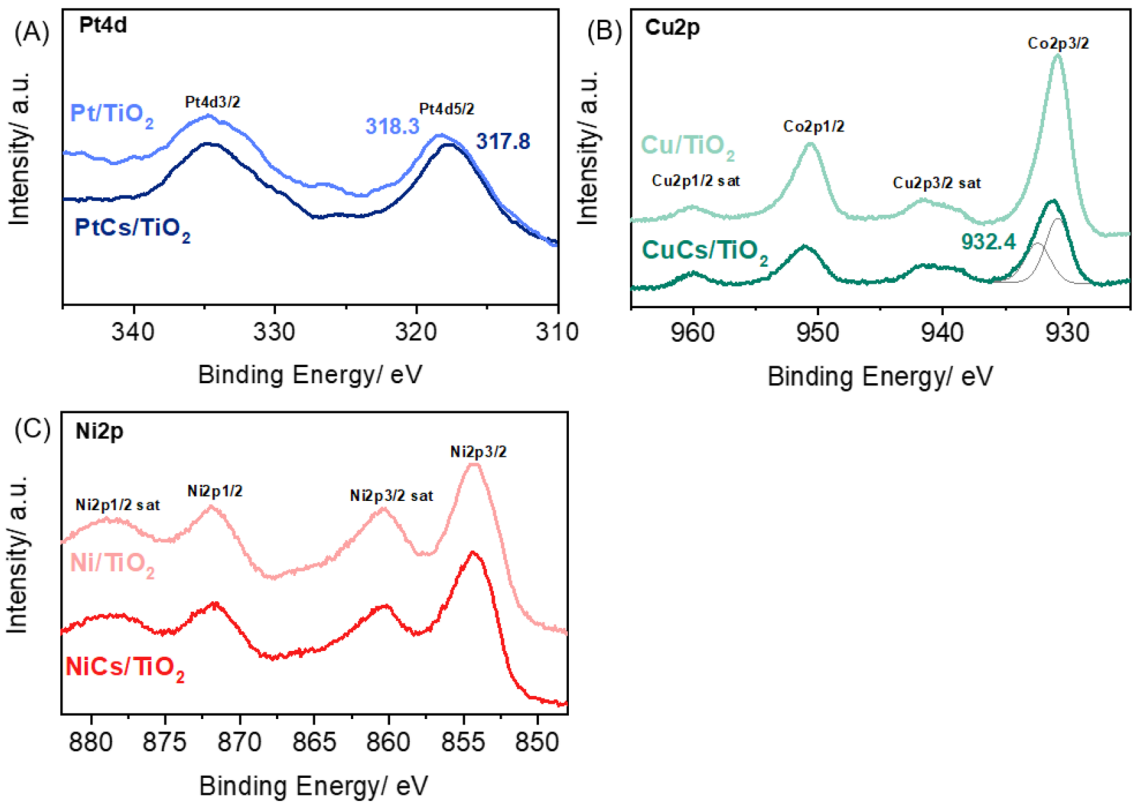

Fig. 5 XPS spectra of Pt/TiO_2–$PtCs/TiO_2$ (**a**), Cu/TiO_2–$CuCs/TiO_2$ (**b**) and Ni/TiO_2–$NiCs/TiO_2$ (**c**)

transfer from the catalyst to the reactants, thus enhancing their adsorption and activation [23].

Finally, Fig. 5b shows the Cu2p spectrum for Cu/TiO_2 and $CuCs/TiO_2$. In the case of Cu/TiO_2, the characteristic spectrum of CuO can be observed [38]. However, when the sample is doped with Cs, the signal related to Cu2p3/2 is broader. This suggest that Cs is helping to stabilize another type of copper with higher binding energy. This information can be correlated with the HR-TEM images of $CuCs/TiO_2$ sample where Cu_4O_3 type species can be observed but are not present in the non-doped catalyst. The interplay among the different copper species reflects Cu redox behaviour which is also helpful to undertake CO_2 activation and push forward the RWGS reaction [39].

3.6 Catalytic Activity

The catalytic performance of the six samples is presented in Figs. 6 and 7. The Ni/TiO_2 catalyst presents the highest CO_2 conversion but exhibits poor CO selectivity due to its tendency to form methane, in fair agreement with previous studies [40]. Ni/TiO_2 catalyst have been reported before, achieving remarkable CO_2 conversions and CH_4 selectivity [41]. However, the addition of Cs significantly alters the selectivity towards CO, particularly at low temperatures. This reinforces our hypothesis that Cs suppresses methanation in Ni-based catalysts opening a new route for typical Sabatier catalysts to become switchable Methanation/RWGS systems as reported by our team [9]. Cs addition results in an electron-rich surface favouring CO desorption and hence the selectivity towards CO [42]. CO_2 conversion is also affected being significantly lower in comparison to the non-doped sample. This may be explained by the lower dispersion and higher particle size of Ni, as it was discussed in the HR-TEM section.

On the other hand, both the Cu/TiO_2 and $CuCs/TiO_2$ catalysts exhibit nearly 100% CO selectivity. However, it is noticeable that the non-doped Cu catalyst presents low CO_2 conversion, while the addition of Cs remarkably enhances it.

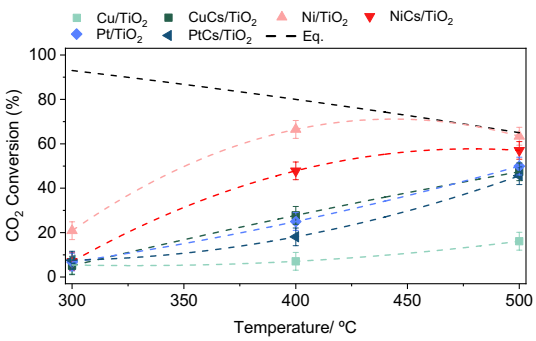

Fig. 6 CO_2 conversion of the studied catalysts at 300, 400 and 500 °C

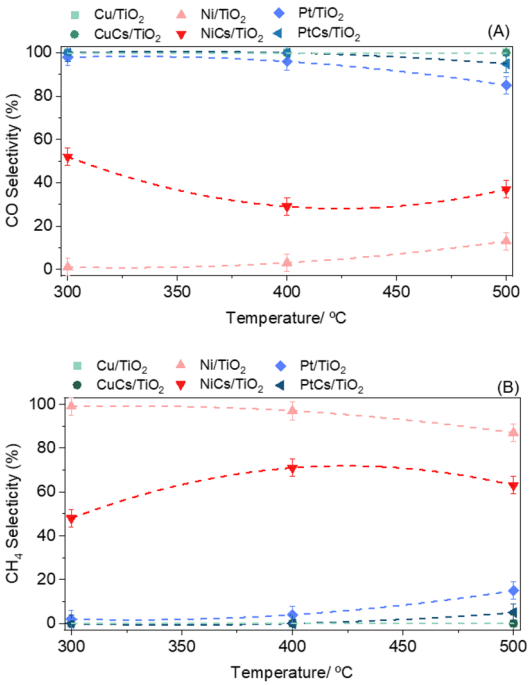

Fig. 7 Selectivity for **A** CO and **B** CH_4 of the six catalysts at 300, 400 and 500 °C

The low activity for the non-doped catalysts can be related to Cu small particles not being accessible for reactants. As can be seen in the particles size distribution from HR-TEM, half of the particles measured for this samples are 1 nm size. It can be thought that encapsulation of these particles by the TiO_2 due to SMSI effect is taking place, avoiding reactants to enter in contact with copper active sites. This has been previously observed in surface reconstruction phenomena on Cu/TiO_2 nanotubes for CO_2 conversion [43].

In the case of $CuCs/TiO_2$ catalyst, the CuO clusters are bigger and even though SMSI effect can be also occurring in this sample, the total encapsulation of the active phase is not taking place. In fact, SMSI effect can improve the catalytic activity of the system. Zhang et al. [44] studied the SMSI effect by the introduction of oxygen vacancies in Cu/TiO_2 catalyst for CO_2 hydrogenation reactions, concluding that controlling this effect can promote CO_2 adsorption and activation because of the new interface generated between Cu and TiO_2. In addition, the presence of Cu_4O_3 species observed in HR-TEM is supported by XPS, as the addition of Cs seems to help the stabilization of a different type of copper species with lower electron density. The presence of this new specie could be the reason of the difference in the catalytic activity of the two copper base catalyst, enhancing CO_2 adsorption and activation [42].

Selectivity is the key factor in the RWGS specially at low-temperatures where methanation is favoured. Specific activities for products formation provides a clear basis for

performance comparison among the studied multicomponent systems. Figure 8 shows specific activity towards CO and CH_4. The positive promotion effect of Cs is more clearly seen in these graphs. When Cs is added to Cu catalyst, its specific activity follows the trend of the Pt-Cs catalysts. On the other hand, it should be remarked again how the CH_4 production significantly drops upon Cs addition in the Ni catalysts. Overall Pt-systems present the best activity/selectivity balance, but it is worth nothing that the Cs-promoted Cu catalysts display comparable and even higher CO production capacity with very similar CO_2 conversion values making the multicomponent $CuCs/TiO_2$ an economically appealing option for low-temperature RWGS units. To further set the context of our multicomponent catalysts in the RWGS scenario, Table 2, provides a comparison of the catalytic performance of our systems versus reported catalysts in literature tested under comparable conditions. Overall, the table showcases the potential of our multicomponent catalysts that present remarkable performance standing out within the so far reported systems for this reaction.

4 Conclusion

This study showcases an effective strategy to design low-temperature RWGS catalysts using Cs-doped multicomponent catalysts. The addition of Cs to all catalysts resulted in

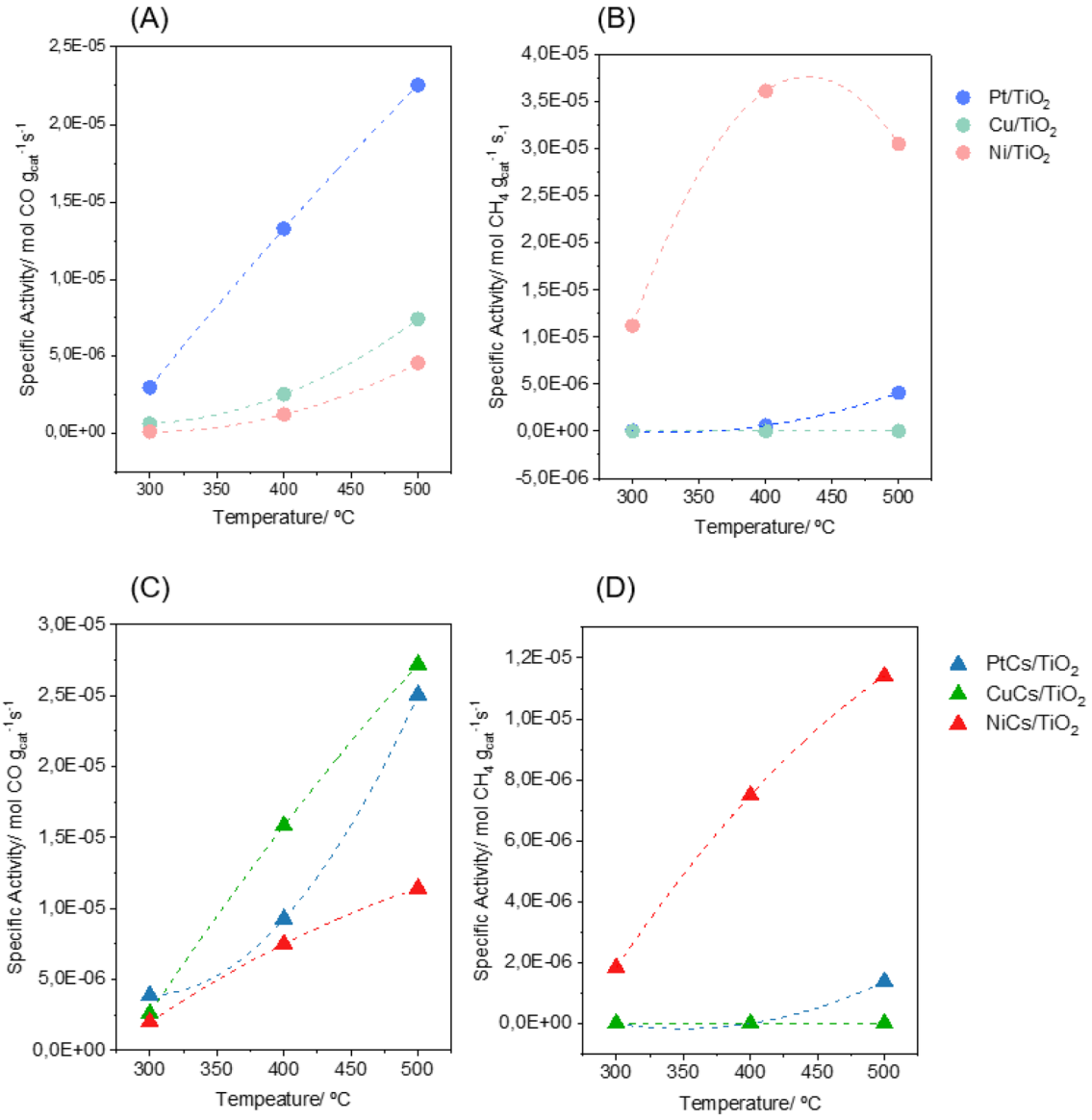

Fig. 8 Specific activity towards CO for Pt/TiO_2, Cu/TiO_2 Ni/TiO_2 (**a**) and Cs-doped catalysts (**c**) and towards CH_4 for Pt/TiO_2, Cu/TiO_2 Ni/TiO_2 (**b**) and Cs-doped catalysts (**d**)

Table 2 Catalytic activity comparison with literature findings

Catalyst	H_2:CO_2 ratio	Temperature	CO_2 conversion (%)	CO selectivity (%)	Space velocity ($ml/g_{cat}/h$)	References
Pt/TiO_2	4:1	400	25	96	30.000	This work
$PtCs/TiO_2$	4:1	400	18	100	30.000	This work
Cu/TiO_2	4:1	400	7	100	30.000	This work
$CuCs/TiO_2$	4:1	400	28	100	30.000	This work
Ni/TiO_2	4:1	400	66	3	30.000	This work
$NiCs/TiO_2$	4:1	400	48	29	30.000	This work
Ni/CeO_2	4:1	400	69	28	60.000	[45]
Mn/CeO_2	4:1	400	8	100	60.000	[45]
$Mo/\gamma\text{-}Al_2O_3$	1:1	600	34	97	30.000	[46]
Pt/TiO_2	1:1	400	21	65	6000	[47]
Au/CeO_2	3:1	400	28	100	12.000	[48]
$Cu/\beta\text{-}Mo_2C$	2:1	500	28	99	300.000	[49]
PtK/Mullite	1:1	550	31	99	30.000	[50]
$Fe–Mo–Al_{12}O_3$	1:1	600	45	100	30.000	[7]

improved catalytic performance at low temperatures. The Cs promoter effectively inhibited the methanation reaction, favoring the production of CO. This effect can be clearly observed in the Ni/TiO_2 catalyst. While the non-doped catalysts present a 100% selectivity towards CH_4, the addition of Cs undoubtedly shift this behavior, reducing this value to less than 50%. Addition of Cs to Cu/TiO_2 catalyst doubled its CO_2 conversion reaching almost the activity of Pt/TiO_2. Overall, the observed trends in the catalytic activity of the different catalysts may be attributed to Cs modifying the redox and structural properties of the catalytic systems. Based on TPR and HR-TEM results, the electron-donor capacity of Cs towards the different species is evidenced. This effect can be better analyzed by XPS over Pt and Cu based catalysts. An increase in electron density over Pt species due to the presence of Cs can be observed. This could facilitate de activation an adsorption of the reactants. For copper catalysts, the addition of Cs seems to stabilize a different type of copper active sites, enhancing remarkably its catalytic performance. Additionally, Cs may favor stronger support-metal interactions and could also facilitate the adsorption and activation of CO_2 molecules.

Outperforming Pt as champion active phase is hard and our data indicate that Pt-systems display the best activity/selectivity balance. Nonetheless, the Cs-promoted Cu catalysts reach comparable and even higher CO production specific activity with very similar CO_2 conversion values making the multicomponent $CuCs/TiO_2$ an economically appealing alternative for low-temperature RWGS units. Hence, further refinement of our $CuCs/TiO_2$ could lead to promising results and direct application on advanced CO_2 conversion units that will be crucial in modern net-zero industrial environments.

Supplementary Information The online version contains supplementary material available at https://doi.org/10.1007/s11244-024-01935-7.

Acknowledgements This work has been supported by the grant FJC2021-047672-I co-financed by MCIN/AEI/10.13039/501100011033 and the European Union NextGenerationEU/PRTR funds. Authors also acknowledge support from the grants PID2019-108502RJ-I00 and grant IJC2019-040560-I both funded by MCIN/AEI/ 10.13039/501100011033 as well as the projects NICER-BIOFUELS (ref: PLEC2021-008086), sponsored by MCIN/AEI/10.13039/501100011033 Next Generation Europe and SMART-FTS (ref: PID2021-126876OB-I00), sponsored by MCIN/AEI /10.13039/501100011033 and European Union ERDF.

Authors Contribution G. Torres-Sempere: conceptualisation, methodology, validation, formal analysis, investigation, writing—original draft. J.Gonzalez-Arias: data curation, review. A. Penkova: Investigation, formal analysis. J.L. Santos-Muñoz: Investigation, methodology, review. L.F. Bobadilla: supervision, review. J. A. Odriozola: formal analysis, resources, funding acquisition. L. Pastor-Pérez: resources, supervision, review. Tomás R. Reina: conceptualisation, methodology, resources, writing—review & editing, supervision, project administration, funding acquisition.

Funding Funding for open access publishing: Universidad de Sevilla/CBUA.

Data Availability Not applicable.

References

1. Chávez-Rocha R, Mercado-Sánchez I, Vargas-Rodriguez I et al (2023) Modeling adsorption of CO2 in rutile metallic oxide surfaces: implications in CO2 catalysis. Molecules. https://doi.org/10.3390/molecules28041776
2. Zhang R, Hu D, Zhou Y et al (2023) Tuning ionic liquid-based catalysts for CO2 conversion into quinazoline-2,4(1H,3H)-diones. Molecules. https://doi.org/10.3390/molecules28031024
3. Mikkelsen M, Jørgensen M, Krebs FC (2010) The teraton challenge. A review of fixation and transformation of carbon dioxide. Energy Environ Sci 3:43–81. https://doi.org/10.1039/b912904a
4. Mihet M, Dan M, Lazar MD (2022) CO2 hydrogenation catalyzed by graphene-based materials. Molecules. https://doi.org/10.3390/molecules27113367
5. Su X, Yang X, Zhao B, Huang Y (2017) Designing of highly selective and high-temperature endurable RWGS heterogeneous catalysts: recent advances and the future directions. J Energy Chem. https://doi.org/10.1016/j.jechem.2017.07.006
6. Chen Z, Liang L, Yuan H et al (2021) Reciprocal regulation between support defects and strong metal-support interactions for highly efficient reverse water gas shift reaction over Pt/TiO2 nanosheets catalysts. Appl Catal B. https://doi.org/10.1016/j.apcatb.2021.120507
7. Kharaji AG, Shariati A, Takassi MA (2013) A novel γ-alumina supported fe-mo bimetallic catalyst for reverse water gas shift reaction. Chin J Chem Eng. https://doi.org/10.1016/S1004-9541(13)60573-X
8. Daza YA, Kuhn JN (2016) CO2 conversion by reverse water gas shift catalysis: comparison of catalysts, mechanisms and their consequences for CO2 conversion to liquid fuels. RSC Adv. https://doi.org/10.1039/c6ra05414e
9. Le Saché E, Pastor-Pérez L, Haycock BJ et al (2020) Switchable catalysts for chemical CO2 recycling: a step forward in the methanation and reverse water-gas shift reactions. ACS Sustain Chem Eng 8(11):4614–4622. https://doi.org/10.1021/acssuschemeng.0c00551
10. Centi G, Quadrelli EA, Perathoner S (2013) Catalysis for CO2 conversion: a key technology for rapid introduction of renewable energy in the value chain of chemical industries. Energy Environ Sci. https://doi.org/10.1039/c3ee00056g
11. Marín-s M, Lobo-andrades L, Azancot L et al (2023) Low-temperature reverse water gas-shift reaction over highly efficient Cu-hydrotalcites: mechanistic insights on the role of malachite phase A. Catal Today. https://doi.org/10.1016/j.cattod.2023.114235
12 Lim HS, Lee M, Kim Y et al (2021) Low-temperature CO2 hydrogenation to CO on Ni-incorporated LaCoO3 perovskite catalysts. J Hydrogen Energy Int. https://doi.org/10.1016/j.ijhydene.2021.02.085
13. Rabee AIM, Zhao D, Cisneros S et al (2023) Role of interfacial oxygen vacancies in low-loaded Au-based catalysts for the low-temperature reverse water gas shift reaction. Appl Catal B. https://doi.org/10.1016/j.apcatb.2022.122083
14. Liu L, Das S, Chen T et al (2020) Low temperature catalytic reverse water-gas shift reaction over perovskite catalysts in DBD plasma. Appl Catal B. https://doi.org/10.1016/j.apcatb.2019.118573
15. Liu Y, Liu D (1999) Study of bimetallic Cu-Ni/γ-Al2O3 catalysts for carbon dioxide hydrogenation. Int J Hydrogen Energy. https://doi.org/10.1016/S0360-3199(98)00038-X
16. Goguet A, Meunier FC, Tibiletti D et al (2004) Spectrokinetic investigation of reverse water-gas-shift reaction intermediates over a Pt/CeO2 catalyst. J Phys Chem B. https://doi.org/10.1021/jp047242w
17. Kusama H, Bando KK, Okabe K, Arakawa H (2001) CO2 hydrogenation reactivity and structure of Rh/SiO2 catalysts prepared from acetate, chloride and nitrate precursors. Appl Catal A:Gen. https://doi.org/10.1016/S0926-860X(00)00576-7
18. Kim SS, Lee HH, Hong SC (2012) The effect of the morphological characteristics of TiO2 supports on the reverse water-gas shift reaction over Pt/TiO2 catalysts. Appl Catal B. https://doi.org/10.1016/j.apcatb.2012.02.023
19. Inoue T, Iizuka T (1986) Hydrogenation of carbon dioxide and carbon monoxide over supported Rhodium catalysts under 10 bar pressure. J Chem Soc Faraday Trans. https://doi.org/10.1039/F19868201681
20. Pettigrew DJ, Trimm DL, Cant NW (1994) The effects of rare earth oxides on the reverse water-gas shift reaction on palladium/alumina. Catal Lett. https://doi.org/10.1007/BF00806061
21. Bobadilla LF, Santos JL, Ivanova S et al (2018) Unravelling the role of oxygen vacancies in the mechanism of the reverse water-gas shift reaction by operando DRIFTS and ultraviolet-visible spectroscopy. ACS Catal. https://doi.org/10.1021/acscatal.8b02121
22. Liu X, Pajares A, CalinaoMatienzo DD et al (2020) Preparation and characterization of bulk MoXC catalysts and their use in the reverse water-gas shift reaction. Catal Today. https://doi.org/10.1016/j.cattod.2019.11.011
23. Pastor-Pérez L, Baibars F, Le Sache E et al (2017) CO2 valorisation via reverse water-gas shift reaction using advanced Cs doped Fe-Cu/Al2O3 catalysts. J CO2 Util. https://doi.org/10.1016/j.jcou.2017.08.009
24 Mine S, Yamaguchi T, Ting KW et al (2021) Reverse water-gas shift reaction over Pt/MoOx/TiO2: reverse Mars-van Krevelen mechanismviaredox of supported MoOx. Catal Sci Technol. https://doi.org/10.1039/d1cy00289a
25. Yang X, Su X, Chen X et al (2017) Promotion effects of potassium on the activity and selectivity of Pt/zeolite catalysts for reverse water gas shift reaction. Appl Catal B. https://doi.org/10.1016/j.apcatb.2017.05.067
26. Zhou R, Rui N, Fan Z, Liu C-J (2016) Effect of the structure of Ni/TiO2 catalyst on CO2 methanation. Int J Hydrogen Energy. https://doi.org/10.1016/j.ijhydene.2016.08.093
27. Kim SS, Park KH, Hong SC (2011) A study on HCHO oxidation characteristics at room temperature using a Pt/TiO2 catalyst. Appl Catal A. https://doi.org/10.1016/j.apcata.2011.03.018
28. Fernandes Machado NRC, Santana VS (2005) Influence of thermal treatment on the structure and photocatalytic activity of TiO2 P25. Catal Today. https://doi.org/10.1016/j.cattod.2005.07.022
29. Krýsa J, Keppert M, Štengl V, Šubrt J (2004) The effect of thermal treatment on the properties of TiO2 photocatalyst. Matter Chem Phys. https://doi.org/10.1016/j.matchemphys.2004.03.021
30. Di L, Xu Z, Wang K, Zhang X (2013) A facile method for preparing Pt/TiO2 photocatalyst with enhanced activity using dielectric barrier discharge. Catal Today. https://doi.org/10.1016/j.cattod.2013.03.025
31. Zhang S, Wang J, Wang X (2008) Effect of calcination temperature on structure and performance of Ni/TiO2-SiO2 catalyst for CO2 reforming of methane. J Nat Gas Chem. https://doi.org/10.1016/S1003-9953(08)60048-1
32. Chen I, Chen FL (1990) Effect of alkali and alkaline-earth metals on the resistivity to coke formation and sintering of nickel-alumina catalysts. Chi J Chem Eng 29:534–539
33. Petrik IS, Krylova GV, Kelyp OO et al (2015) XPS and TPR study of sol-gel derived M/TiO2 powders (M=Co, Cu, Mn, Ni). Him Fiz Tehnol Poverhni. https://doi.org/10.15407/hftp06.02.179
34. Peng J, Wang S (2007) Performance and characterization of supported metal catalysts for complete oxidation of formaldehyde at low temperatures. Appl Catal B. https://doi.org/10.1016/j.apcatb.2006.12.012

35. Zhao D, Lü D, Zang Y, Zhao X (1997) Spillover in heterogeneous catalysis. Prog Chem 9:759–788
36. Liang H, Zhang Y, Liu Y (2008) Three-dimensionally ordered macro-porous Pt/TiO2 catalyst used for water-gas shift reaction. J Nat Gas Chem. https://doi.org/10.1016/S1003-9953(09)60017-7
37. Torres-Sempere G, Blay-Roger R, Luque-Álvarez LA et al (2023) Subnanometric Pt clusters dispersed over Cs-doped TiO2 for CO2 upgrading via low-temperature RWGS: operando mechanistic insights to guide an optimal catalyst design. J Mater Chem A. https://doi.org/10.1039/d3ta05482a
38. Naumkin AV, Kraut-Vass A, Gaarenstroom SW, Powell CJ (2000) NIST X-ray photoelectron spectroscopy database. NIST Standard Reference Database
39 Yang L, Pastor-Pérez L, Villora-Pico JJ et al (2021) Highly active and selective multicomponent Fe-Cu/CeO2-Al2O3 catalysts for CO2 upgrading via RWGS: impact of Fe/Cu ratio. ACS Sustain Chem Eng. https://doi.org/10.1021/acssuschemeng.1c03551
40. Lan L, Daly H, Jiao Y et al (2021) ScienceDirect comparative study of the effect of TiO 2 support composition and Pt loading on the performance of Pt/TiO2 photocatalysts for catalytic photoreforming of cellulose. Int J Hydrogen Energy. https://doi.org/10.1016/j.ijhydene.2021.06.043
41. Li L, Zeng W, Song M et al (2022) Research progress and reaction mechanism of CO2 methanation over Ni-based catalysts at low temperature: a review. Catalysts. https://doi.org/10.3390/catal12020244
42. Zhang Q, Pastor-Pérez L, Jin W et al (2019) Understanding the promoter effect of Cu and Cs over highly effective B-Mo2C catalysts for the reverse water-gas shift reaction. Appl Catal B. https://doi.org/10.1016/j.apcatb.2018.12.023
43. Liu C, Nauert SL, Alsina MA et al (2019) Role of surface reconstruction on Cu/TiO2 nanotubes for CO2 conversion. Appl Catal B. https://doi.org/10.1016/j.apcatb.2019.117754
44. Zhang C, Wang L, Etim UJ et al (2022) Oxygen vacancies in Cu/TiO2 boost strong metal-support interaction and CO2 hydrogenation to methanol. J Catal. https://doi.org/10.1016/j.jcat.2022.06.026
45. Dai B, Zhou G, Ge S et al (2017) CO2 reverse water-gas shift reaction on mesoporous M-CeO2 catalysts. Can J Chem Eng. https://doi.org/10.1002/cjce.22730
46. Kharaji AG, Shariati A, Ostadi M (2014) Development of Ni-Mo/Al2O3 catalyst for reverse water gas shift (RWGS) reaction. J Nanosci Nanotechnol. https://doi.org/10.1166/jnn.2014.8962
47. Chen X, Su X, Duan H et al (2017) Catalytic performance of the Pt/TiO2 catalysts in reverse water gas shift reaction: controlled product selectivity and a mechanism study. Catal Today. https://doi.org/10.1016/j.cattod.2016.03.020
48. Zhu X, Qu X, Li X et al (2016) Selective reduction of carbon dioxide to carbon monoxide over Au/CeO2 catalyst and identification of reaction intermediate. J Catal. https://doi.org/10.1016/S1872-2067(16)62538-X
49. Zhang X, Zhu X, Lin L et al (2017) Highly dispersed copper over β-Mo2C as an efficient and stable catalyst for the reverse water gas shift (RWGS) reaction. ACS Catal. https://doi.org/10.1021/acscatal.6b02991
50. Liang B, Duan H, Su X et al (2017) Promoting role of potassium in the reverse water gas shift reaction on Pt/mullite catalyst. Catal Today. https://doi.org/10.1016/j.cattod.2016.02.051